RSC Advances

PAPER

Surface interaction of WO_3 nanocrystals with NH_3. Role of the exposed crystal surfaces and porous structure in enhancing the electrical response

Cite this: *RSC Adv.*, 2014, **4**, 11012

Massimiliano D'Arienzo,*[a] Lidia Armelao,[b] Claudio Maria Mari,[a] Stefano Polizzi,[c] Riccardo Ruffo,[a] Roberto Scotti[a] and Franca Morazzoni[a]

Received 15th November 2013
Accepted 7th February 2014

DOI: 10.1039/c3ra46726k

www.rsc.org/advances

We report on the surface interaction between NH_3 and WO_3 nanoparticles having different exposed surfaces or different porous structure, to identify the relative importance of exposed crystal surfaces, porous architecture, and specific surface area in the oxide sensing properties. WO_3 nanocrystals with tailored morphology and definite prominent surfaces were synthesized by hydrothermal reactions. In parallel, inverted opal macroporous WO_3 films have been prepared by a *one-step* sol–gel procedure, and WO_3 hierarchical layers have been obtained by an innovative *one-step* dual-templating strategy which leads to macropores and mesopores simultaneously. The performances of WO_3 samples in NH_3 sensing, indicate that high-energy surfaces result in a significant improvement of the electrical response. Enhanced porous structure and high surface area are not enough to produce high electrical response, while their synergistic combination with tailored crystal faceting appears effective. XPS survey performed on shape controlled WO_3 nanocrystals demonstrated that, upon interaction with NH_3, oxidized nitrogen atoms represent the prevalent species on the surface of rectangular (WO_3-RE) nanocrystals with highly exposed high-energy {020} and {002} facets. Conversely, in the case of rectangular platelets (WO_3-SS) and square platelets (WO_3-RS) with very low surface area of high-energy surfaces, N–H surface groups are predominant. These results suggest that {020} and {002} crystal surfaces provide privileged reactive sites for ammonia oxidation and therefore they play a key role in driving the sensing properties of the WO_3 layers.

Introduction

The detection and monitoring of gases by solid state sensors play an important role in the control of chemical processes, environmental monitoring and personal safety.[1–5] Metal oxides have been extensively employed as gas sensing materials due to their low cost and high compatibility with microelectronic processing.[1–9] Among semiconductor metal-oxides, WO_3 is considered as one of the most promising materials for toxic gas detection,[10,11] in particular for ammonia detection.[12,13,22–24] Extensive scientific and engineering research is still active in this field, focused on enhancing the electrical response and optimizing the response rate, the gas selectivity and long-term stability.[14,15] To fulfill all these objectives a deeper knowledge of the WO_3 sensing mechanism is necessary.

The sensing properties of semiconductor oxides are in general determined by the redox interaction of the gas molecules with the surface.[1–3] A very effective charge transfer is provided by the nanometric oxide particles, with a size comparable to the thickness of the space-charge region.[16,17] High interconnectivity between the particles facilitates electron mobility.[18,19] Moreover high surface area favors the gas–oxide interaction[18,20] and, in particular, meso and macroporous structures significantly improve gas diffusion throughout the layer and consequently the sensing performance.[20,21] The sensor response can significantly be enhanced by noble metals centres, *e.g.* Cr and Pt, homogeneously dispersed into the oxide matrix, which catalyze the electron transfer between gas molecules and the semiconductor.[22–24] In this context, using an innovative *one-step* sol–gel procedure, we recently prepared macroporous undoped and Cr- or Pt-doped WO_3 inverted opal films to be employed as NH_3 sensor materials.[21] The WO_3 semiconductor layers revealed considerable electrical response upon exposure to NH_3, even at relatively low operating temperatures, showing a much higher sensitivity than the mesoporous layers. Such a behavior was attributed to the capability of the macroporous architecture in promoting

[a]*INSTM, Department of Materials Science, University of Milano-Bicocca, Via R. Cozzi 53, I-20125 Milano, Italy. E-mail: massimiliano.darienzo@mater.unimib.it*

[b]*IENI – CNR and INSTM, Department of Chemical Sciences, University of Padova, Via F. Marzolo 1, I-35131 Padova, Italy*

[c]*Department of Molecular Sciences and Nanosystems, University Ca' Foscari of Venezia, Via Torino 155/b, I-30172 Venezia, Italy*

the effective gas diffusion within the entire sensing layer, leading to higher sensitivity than that of conventional sol–gel films with identical composition.[21]

Recently, several studies have demonstrated that the electrical response and the selectivity of nanostructured metal-oxide gas sensors are significantly affected by the shape of the nanocrystals and specifically by their exposed crystal surfaces.[10,20,25,26] In this perspective, efforts have been devoted to the development of morphology controlled semiconductor oxides with specific exposed crystal surfaces.[20,25–27] For instance, Han *et al.*[26] demonstrated that shape controlled WO_3 nanocrystals with highly exposed {020} facets exhibit higher sensitivity towards 1-butylamine compared to nanoparticles with other prominent facets. The differences in the gas sensing capability were attributed to the presence of coordinatively unsaturated cations on the {020} surfaces, *i.e.* five and four-fold coordinated W ions, which could effectively chemisorb both oxygen species (*e.g.* O^{2-}, O^-, $O_2^{-\bullet}$) and the target gases.[26] Although not referring to the gas-sensing, Liu *et al.*[27] indicated that the surface energy of crystal faces in shape controlled WO_3 nanocrystals with monoclinic crystal structure follows the order {002} (1.56 J m^{-2}) > {020} (1.54 J m^{-2}) > {200} (1.43 J m^{-2}) and suggested that {002} and {020} are the most active in surface-mediated reactions.

From this background, it is evident that the porous structure, the specific surface area and the exposed crystal surfaces can dramatically influence the sensing properties of WO_3 nanocrystals. Thus, in our opinion, the comparison among the sensing behavior of WO_3 nanoparticles with different morphology (*i.e.* specific shape and exposed surfaces) or with different meso/macroporous structure may help to evaluate the relative contributions of the oxide facets, of the porous architecture and of the specific surface area to the gas sensing properties.

In order to investigate the effect of the crystal facets on the sensing response, WO_3 nanocrystals with tailored morphology and definite prominent surfaces were synthesized by previously reported hydrothermal reactions[28–30] and used to produce films. In parallel, to study the influence of the porous structure and of the surface area, we prepared macroporous WO_3 inverted opal films according to the above mentioned *one-step* procedure[21] and hierarchical tungsten oxide layers by an innovative *one-step* dual-templating (block copolymer Pluronic P123 and colloidal PMMA microspheres) strategy which guarantees the simultaneous presence of macropores and mesopores.

The sensing performances of the samples toward NH_3 were compared in order to suggest a rationale for the relative importance of the crystal facets and of the porous structure in determining the sensing properties. Moreover, to gain deeper insight into the role played by the exposed surfaces at the electronic level in the sensing mechanism, a comprehensive XPS investigation on shape controlled WO_3 nanocrystals was performed. To the best of our knowledge, this study represents the first investigation on the crystal surface involvement in the ammonia sensing mechanism and may shed some light on how the crystal facet engineering can help to design more efficient WO_3 sensors.

Experimental

Chemicals

Methyl methacrylate (MMA, 99%), poly(alkylene oxide) block copolymer ($HO(CH_2CH_2O)_{20}(CH_2CH(CH_3)O)_{70}(CH_2CH_2O)_{20}OH$ ($EO_{20}PO_{70}EO_{20}$), Pluronic P123) 2,20-azobis (2-methyl-propionamidine)dihydrochloride (97%), ammonium meta-tungstate ($(NH_4)_6H_2W_{12}O_{40}$, 99.9%), sodium tungstate ($Na_2WO_4 \cdot 2H_2O$), hydrochloric acid (HCl) and oxalic acid ($C_2H_2O_4 \cdot 2H_2O$) were all purchased from Aldrich and used without further purification.

Synthesis of shape controlled WO_3 nanocrystals and preparation of thin films

The preparation of morphology controlled WO_3 nanoparticles was performed according to previously reported procedures.[28–31] WO_3 nanoparticles with cubic, rectangular, rectangular platelet and square-like platelet shapes were prepared and used to fabricate films.

WO_3 rectangular nanocrystals (WO_3-RE) were synthesized by dissolving 0.79 g of $Na_2WO_4 \cdot 2H_2O$ in 45 mL of distilled water at 70 °C. Then 1 mL of 10 M HCl solution was added, and the resulting suspension was aged at 70 °C overnight. The yellow solid was recovered by centrifugation, washed with distilled water and acetone, and finally calcined at 400 °C for 2 h in air.[28]

To synthesize WO_3 square-like platelets (WO_3-SS), 6.6 g of $Na_2WO_4 \cdot 2H_2O$ were dissolved in 100 mL of water, and HCl 37% m m^{-1} was added drop by drop to this solution until pH = 1. The white precipitate obtained was dissolved by adding oxalic acid (0.4 g in 30 mL of H_2O). The resulting transparent solution was finally transferred into 25 mL Teflon-lined stainless steel autoclave (filling factor 75%) and maintained at 180 °C for 24 h to obtain the final product.[29]

Rectangular WO_3 platelets (WO_3-RS) were obtained through the dissolution of 1 g $Na_2WO_4 \cdot 2H_2O$ in 20 mL of water under mild stirring, followed by the addition of 2 M HCl until a pale yellow precipitate was formed. The solid was recovered by centrifugation, transferred into 60 mL of 2 M HCl solution and the mixture was stirred for 24 h at 40 °C. Subsequently, 48 mL of this suspension were transferred into a Teflon lined stainless steel autoclave (volume 60 mL) and treated at 200 °C for 5 h. After naturally cooling to room temperature, the product was collected by centrifugation, washed with water and acetone, dried at 80 °C for 10 h and finally calcined at 500 °C in air for 2 h.[30]

Hereafter, WO_3 nanoparticles with cubic, rectangular, square-like platelet and rectangular platelet shapes will be labeled as WO_3-RE, WO_3-SS and WO_3-RS, respectively.

The films for the sensing measurements were prepared by simply depositing few drops of WO_3 paste (consisting of WO_3 nanoparticles mixed with ethanol) onto Suprasil quartz slides (20 × 20 mm, 0.25 mm thickness).

Preparation of WO_3 thin films with controlled porous architecture

Synthesis of polymethylmethacrylate spheres. The aqueous suspension of monodispersed poly(methyl methacrylate)

(PMMA) microspheres (∅ = 450 ± 5 nm) was prepared according to the Schroden standard technique.[31]

Preparation of precursor suspension for WO_3 inverted opal films (WO_3-IO). WO_3 precursor suspension was prepared by dissolving 0.3460 g of $(NH_4)_6H_2W_{12}O_{40}$ in 5 mL of the colloidal aqueous suspension of PMMA microspheres as template for the generation of the macroporous structure. The mixture obtained was stirred at room temperature for several minutes until a homogeneous suspension was obtained.

Preparation of precursor suspension for WO_3 macro/mesoporous films (dual templating strategy, WO_3-DP). In a typical preparation, the copolymer Pluronic P123 (1 g) was dissolved in ethanol (10 mL) under magnetic stirring. Then 0.2500 g of $(NH_4)_6H_2W_{12}O_{40}$ and 1 mL of PMMA microspheres were added to this solution. The mixture obtained was stirred at room temperature for several minutes until a homogeneous suspension was obtained. The presence of the block copolymer, is expected to lead to the formation of a structure which contains both macropores derived from the PMMA and mesopores generated by the folding of the polymeric chains of P123.

Film deposition. WO_3-IO films were prepared by the *one-pot* procedure[21] using the dip-coating method. Suprasil quartz slides were used as the substrates.

WO_3-DP films were obtained by a modification of the one-step procedure. In a typical deposition, the substrate was settled vertically into the WO_3 sol phase for several minutes and then withdrawn at the constant rate of 0.8 cm min^{-1}. After deposition the film was dried in air for about 10 min at 60 °C. The above cycle was repeated five times; then the films were annealed at 450 °C (heating rate 2 °C min^{-1}) in air stream (80 cm^3 min^{-1}) for 5 h to fully decompose the organic remnants.

The scheme of the one-step deposition of the macro/mesoporous WO_3 films is reported in Fig. 1. A similar scheme has been reported for the deposition of WO_3 inverse opal films.[21]

Structural and morphological characterization

The preparation of morphology X-ray diffraction (XRD) analysis was performed on WO_3 powdered samples. XRD patterns were collected with a Bruker D8 Advance (Cu Kα radiation) in the range 10–50° 2θ (2θ step 0.025°, count time of 2 s per step).

Specific surface area (SSA) by BET method,[32] desorption cumulative pore volume (DCPV) and pore size distribution of micro- and mesopores (<50 nm) by BJH method[33] were measured by nitrogen physisorption using Quantachrome Autosorb-1 apparatus. The nanopowders were evacuated at 200 °C for 16 h before the analysis.

Scanning electron microscopy (SEM) measurements of the films were performed by a Vega TS5136 XM Tescan microscope in a high-vacuum configuration. The electron beam excitation was 30 kV at a beam current of 25 pA, and the working distance was 12 mm. In this configuration the beam spot was 38 nm. Prior to SEM analysis, samples were gold-sputtered.

High-resolution transmission electron microscopy (HRTEM) and electron diffraction (ED) were performed using a Jeol 3010 apparatus operated at 300 kV with a high-resolution pole piece (0.17 nm point-to-point resolution) and equipped with a Gatan slow-scan 794 CCD camera. Samples were obtained by removing a film portion from the substrates in order to obtain a fine powder sample, then suspended by sonication in 2-propanol. A 5 μL drop of this suspension was deposited on a holey carbon film supported on a 3 mm copper grid for TEM investigation.

Since the shape of WO_3-RE, WO_3-SS and WO_3-RS nanocrystals resembles that of a rectangular parallelepiped, the percentage of their exposed {020} and {002} surfaces was calculated using as geometrical model a rectangular parallelepiped with length l, width w and thickness t (Fig. 2). The average values of l, w and t were evaluated by measuring the sizes of ~100 particles in SEM images and their values were inserted in the following equations:

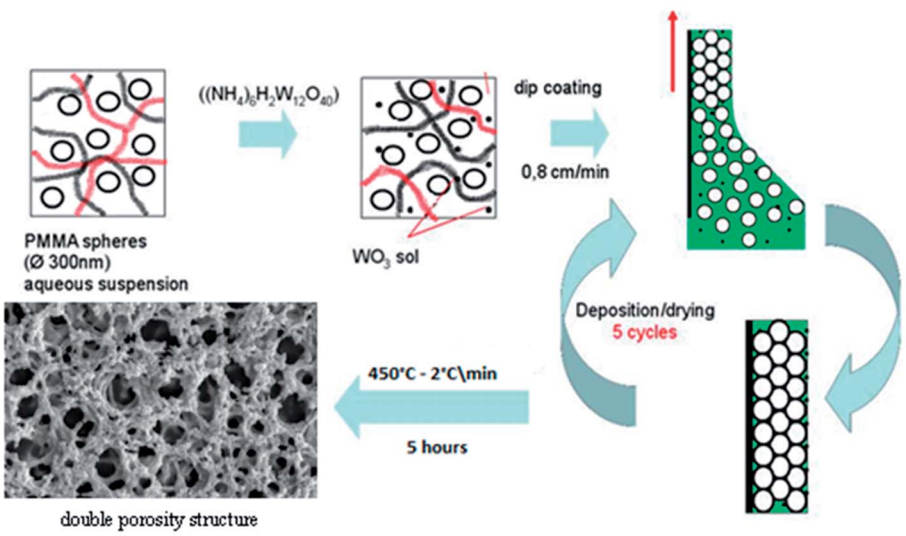

Fig. 1 Scheme of WO_3 macro/mesoporous films preparation by the *one-step* dual templating strategy.

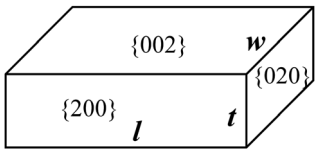

Fig. 2 Geometrical model of WO_3-RE, WO_3-SS and WO_3-RS nanocrystals with the same exposed faces and shape resembling that of a rectangular parallelepiped with rectangular or square basis.

$$\%\, S_{\{020\}} = S_{\{020\}}/(S_{\{020\}} + S_{\{002\}} + S_{\{200\}}) = [2wt/(2wt + 2wl + 2lt)] \times 100 \quad (1)$$

$$\%\, S_{\{002\}} = S_{\{002\}}/(S_{\{002\}} + S_{\{020\}} + S_{\{200\}}) = [2wl/(2wl + 2wt + 2lt)] \times 100 \quad (2)$$

Electrical measurements

Suprasil quartz slides were equipped, before film deposition, with two gold current collectors (20 mm) by the dc sputtering technique. The samples were then placed in a quartz chamber sited in an oven, and the measurements were performed at temperatures ranging from 200 to 325 °C. The electrical resistance was measured by a programmable electrometer controlled by a PC. To dynamically simulate environmental conditions in a controlled and reproducible way, a system based on volumetric gas mixing through mass flow controllers and certified bottles was used. The sensing element was initially equilibrated in dry air (H_2O < 3 ppm, THC < 0.1 ppm) flow (100 mL min^{-1}) at the selected temperature, then NH_3 (range 9.25–74 ppm)–air mixture was introduced (100 mL min^{-1}) up to equilibrium conditions. The different gas mixtures were obtained by dilution of the starting NH_3 (74 ppm)–air mixture using mass flow controllers. The initial resistance conditions of the film were restored by air equilibration, before again introducing the next NH_3–air mixture. The electrical response ($S = R_{AIR}/R_{MIX}$) is defined as the ratio between the film resistance under flowing air (R_{AIR}) and under flowing NH_3–air mixture (R_{MIX}), respectively. All the produced sensors (at least two for each material) were actively working and the response reproducibility (obtained by at least six pulses) was evaluated to be ±13%.

XPS investigation

X-ray photoelectron analysis was performed on WO_3-RE, WO_3-SS and WO_3-RS drop-casted layers heated in air stream (80 cm^3 min^{-1}) or NH_3 (74 ppm)–air stream (80 cm^3 min^{-1}) at 225 °C. Samples were transferred into the fast entry lock system of the XPS vacuum chamber without ambient exposure in order to avoid surface modification or atmospheric contamination. The analysis was performed with a Perkin-Elmer Φ 5600-ci spectrometer using non-monochromatized Al-Kα radiation (1486.6 eV). The examined sample area was 800 μm in diameter and the working pressure lower than 10^{-9} mbar. The spectrometer was calibrated by assuming the binding energy (BE) of the Au $4f_{7/2}$ line at 83.9 eV with respect to the Fermi level. The standard deviation for the BEs values was ±0.2 eV. Survey scans were obtained in the 0–1300 eV range. Detailed scans were recorded for the C1s, O1s, N1s and W4f regions. No further element was detected. The BE shifts were corrected by assigning a value of 284.8 eV to the C1s peak associated with adventitious hydrocarbons.[34] The analysis involved Shirley-type background subtraction, non-linear least-squares curve fitting, adopting Gaussian–Lorentzian peak shapes and peak area determination by integration. The atomic compositions were evaluated from peak areas using sensitivity factors supplied by Perkin-Elmer, taking into account the geometric configuration of the apparatus. Compositional data were averaged over three spots on each sample. The experimental uncertainty on the reported atomic composition values does not exceed ±5%.

Results and discussion

Structural and morphological characterization

XRD and BET analyses were carried out on WO_3 powdered samples, as film characterization can be hardly performed with high accuracy (see Experimental section).

The XRD patterns of the different WO_3 nanocrystals are shown in Fig. 3. The diffraction peaks were assigned to monoclinic WO_3 (JCPDS card no. 43-1035). No secondary phases were detected.

The sharpness of the diffraction pattern observed for the WO_3-RS and WO_3-SS suggests the presence of nanocrystals with large average dimensions and good crystallinity. Conversely, the broadness of the peaks in WO_3-RE, WO_3-IO and WO_3-DP is indicative of nanocrystals with smaller size.

Nitrogen physisorption experiments were performed on all the synthesized WO_3 nanocrystals. Samples are mesoporous

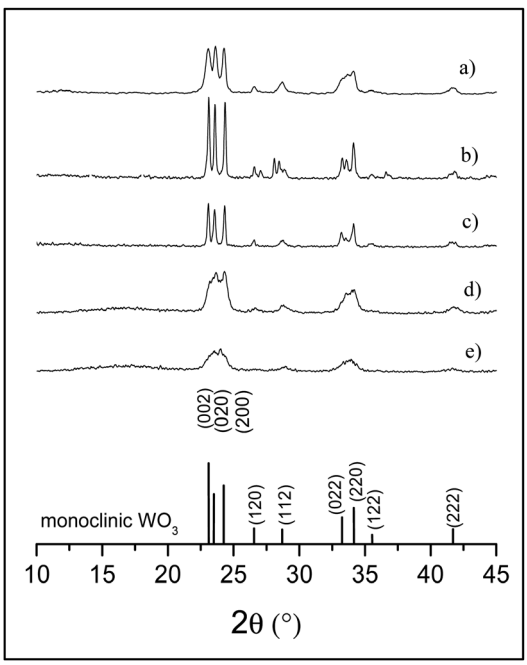

Fig. 3 XRD patterns of: (a) WO_3-RE, (b) WO_3-SS, (c) WO_3-RS, (d) IO and (e) WO_3-DP nanocrystals.

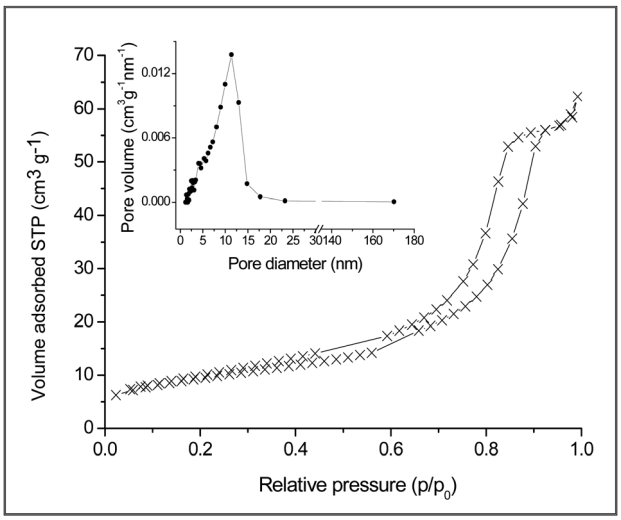

Fig. 4 Adsorption–desorption isotherm at liquid nitrogen temperature for: WO_3-DP nanocrystals. The curve corresponds to a type IV isotherm with capillary condensation in the mesopores. Inset: pore-size distribution.

and show a type IV Brunauer isotherm. As an example, the adsorption–desorption isotherms and the corresponding monomodal pore-size distribution of WO_3-DP nanoparticles are shown in Fig. 4. According to the *t*-plot, no micropores were detected. In particular, the isotherm obtained for WO_3-DP nanoparticles shows a H2 hysteresis loop which is typical of materials with complex structure containing interconnected network of pores having different sizes and shapes. This is in agreement with the broader pore size distribution (between 2 and 15 nm) and the disordered porous architecture of the sample (see SEM investigation).

The specific surface areas (SSA_{BET}) and BJH pore volumes (DCPV) of different WO_3 nanoparticles are reported in Table 1. Using the percentage of the mainly exposed {020}, and {002} crystal faces, their relative SSA_{BET} were also calculated.

Fig. 5 summarizes the results of SEM investigation performed on WO_3 nanoparticles with tailored morphology and porous architecture. The WO_3-RE sample is constituted by very homogeneous rectangular nanoparticles (Fig. 5a) with average length of 300–350 nm, average width of 200–260 nm and thickness of about 100–150 nm.

Square like WO_3 platelets (WO_3-SS sample, Fig. 5b) appear very regular in shape and size, with edge of 430 nm and thickness of about 100–150 nm. WO_3-RS (Fig. 5c) shows instead nanoparticles with smaller dimensions and broader size distribution (average length of 150–250 nm, average width of 100–200 nm and thickness of about 50–100 nm). According to the literature[28–30] and as depicted in the inset schematic models, the WO_3 nanocrystals have two {002} surfaces (top and bottom), and lateral {020} and {200} surfaces.

Based on SEM analysis, average *l*, *w* and *t* values were calculated, which correspond to the sides of the {020} and of {002} faces of WO_3-RE, WO_3-SS and WO_3-RS nanocrystals. The percentages of exposed {020} and {002} crystal facets for WO_3-RE, WO_3-SS and WO_3-RS were calculated according to eqn (1) and (2), and reported in Table 1. These percentages were multiplied for the total the specific surface area of the nanocrystals in order to obtain the relative surface area of {020} and {002}. According to these calculations we can infer that WO_3-RE particles present a surface area of {020} and {002} faces higher than WO_3-SS and WO_3-RS nanocrystals.

SEM images of WO_3-IO highlighted the formation of the inverted opal structure (Fig. 5d).[21] No pore occlusions were detectable and films with extensive homogeneity were obtained. The macropore size measured from the distance between the centers of two neighboring hollow spheres resulted in 300 ± 5 nm, a value lower than the parent PMMA diameter (450 ± 5 nm), due to both the shrinkage of PMMA above the glass transition temperature and the sintering of WO_3.

Fig. 5e and f shows a typical SEM micrograph obtained for WO_3-DP films. A disordered porous architecture with large macropores (above 1 μm) and highly interconnected nanocrystals having small mesopores among them was observed (see TEM investigation). The formation of such a complex structure can be ascribed to the use of two different template agents in alcoholic medium with low water content. In the early stage of the reaction the solution containing the block copolymer Pluronic P123 and ammonium metatungstate first fills up the interstices of the PMMA array. Then, upon drying or solvent evaporation, the interaction of the polar heads and of the ether functions of PEO or PPO blocks with the W^{6+} centers occurs. The complexation of the metal centers by the PEO and the PPO functional blocks alters the micellization behavior of the copolymer, preventing its folding. This effect yields to the

Table 1 Surface parameters and sensing performances of the different WO_3 nanocrystals

Sample	SSA_{BET} ($m^2\ g^{-1}$)	Exposed {002} crystal facets[a] (%)	Exposed {020} crystal facets[a] (%)	SSA_{BET} of exposed {002} crystal facets ($m^2\ g^{-1}$)	SSA_{BET} of exposed {020} crystal facets ($m^2\ g^{-1}$)	Electrical response[b] $S = R_{AIR}/R_{MIX}$ at 225 °C	Electrical response[b] $S = R_{AIR}/R_{MIX}$ at 300 °C
WO_3-RE	140.8	50.9	21.6	71.7	30.4	3.7	2.3
WO_3-SS	5.6	62.7	18.6	3.5	1.0	2.0	3.2
WO_3-RS	31.0	57.8	17.9	18.1	5.6	2.2	2.4
WO_3-IO	13.0	n.d.	n.d.	n.d.	n.d.	3.2	2.9
WO_3-DP	33.5	n.d.	n.d.	n.d.	n.d.	1.8	1.6

[a] Derived from geometrical models. [b] Measured for 74 ppm of NH_3–air mixture.

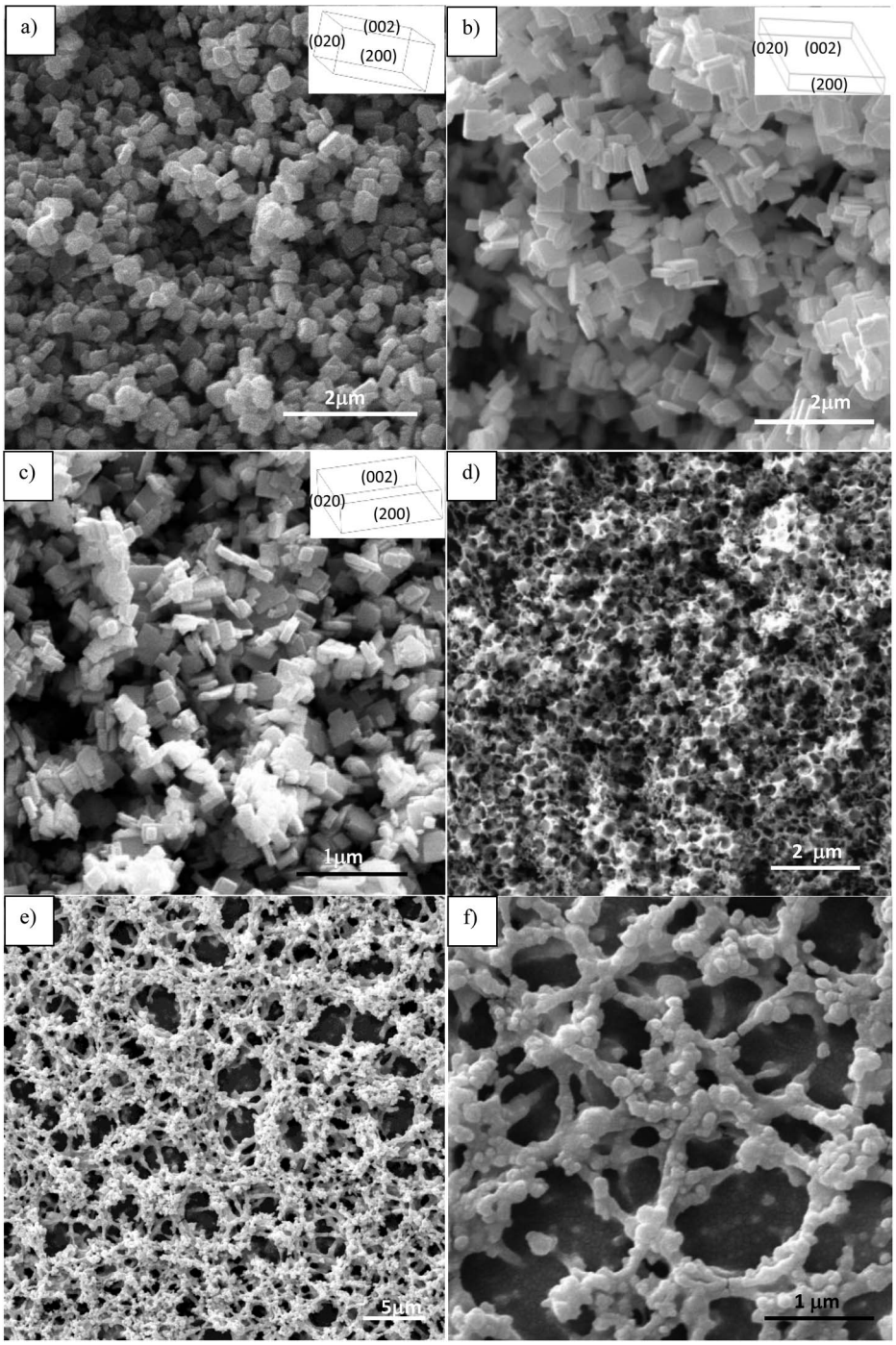

Fig. 5 SEM images of: (a) WO_3-RE, (b) WO_3-SS, (c) WO_3-RS, (d) IO (e) and (f) WO_3-DP nanocrystals.

generation of wormlike disordered mesophases, which may interact with the PMMA microsphere surfaces leading to the formation of meso/macroporous materials with an ill-defined architecture.[35,36]

To better investigate the morphological features of WO_3-IO and WO_3-DP nanocrystals, TEM and HRTEM images were collected (Fig. 6). No amorphous surface layers were detectable. WO_3 inverse opal (WO_3-IO) consists of irregular shaped large nanocrystals (average length > 50 nm) grown around the template spheres (Fig. 6a–c). A representative HRTEM image of a portion of WO_3 nanocrystal is shown in Fig. 6d. The figure inset evidences that the lattice fringes of the nanocrystal have a spacing of 3.74 Å, which reasonably matches the interplanar distance of the {020} surface of the monoclinic tungsten trioxide (ICDD 71-0131).[21] TEM images of WO_3-DP films reveal that WO_3 aggregates are constituted of irregularly shaped interconnected nanocrystals (Fig. 6e and f) with a broad size distribution ranging from 15 to 50 nm, when the statistics is applied to

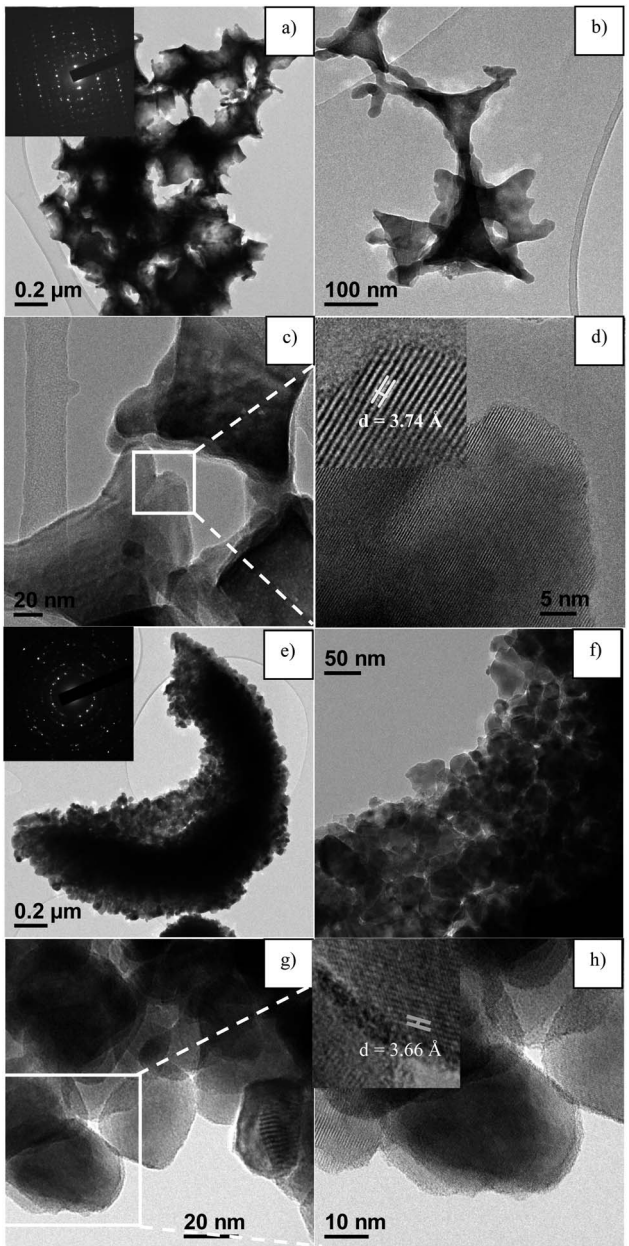

Fig. 6 TEM and HRTEM images of: (a–d) WO_3-DP and (e–h) WO_3-IO nanocrystals. Insets in panel (a) and (e) report the ED patterns collected in selected zones of the WO_3 samples. Insets in panel (d and h) report the crystal structure of WO_3 lattice in WO_3-DP and WO_3-IO, respectively.

about 100 particles. No amorphous phases and internal defects or pores were detectable. Higher magnification reveals that WO_3 nanoparticles (Fig. 6g and h) are separated by small mesopores with dimensions ranging between 5 and 20 nm, in good agreement with the results obtained by nitrogen physisorption. Due to the uneven morphology of the nanocrystals, it is difficult to clearly discriminate the presence of specific crystallographic planes. However, the HRTEM image shows in several nanoparticles (Fig. 6h) lattice fringes with a spacing of 3.66 Å, which matches the interplanar distance of the {200} plane of the monoclinic WO_3.

Electrical measurements

In some our previous papers[21–24] specific reactions and species located at the solid–gas interface were associated with the WO_3 electrical response to ammonia. In particular, we suggested that ammonia molecules chemisorb on both Lewis and Brønsted acidic sites at the WO_3 surface (reactions (3) and (4)). If not simply desorbed, NH_3 can undergo dehydrogenation, mainly through the capture of hydrogen atoms by the oxygen lattice centers (O_O), forming hydroxyl groups. This process, see reactions (5), generates NH_{3-n}^{n-} species (n = 1, 2, 3) which can interact with other NH_{3-n}^{n-} species leading to the formation of molecular nitrogen by reaction (6). Otherwise, they can react with an oxygen center to form nitrogen monoxide, reaction (7), being this the favored path in an oxygen-containing atmosphere. Finally, NH_{3-n}^{n-} species may reduce NO to N_2O by reaction (8).

The whole process is described as follows:

$$NH_3 \rightleftarrows M - NH_3 \quad (M = W) \tag{3}$$

$$NH_3 + M - OH \rightleftarrows M - O^-NH_4^+ \quad (M = W) \tag{4}$$

$$2NH_3 + 6O_O \rightleftarrows \begin{array}{l} \text{reaction (7)} \\ \uparrow\uparrow \\ 2NH_{3-n}^{n-} + 2nO_OH + \ 6 - 2n\ O_O \ \overset{+2NO}{} \ \text{reaction (9)} \\ \downarrow\downarrow \\ \text{reaction (8)} \end{array} \tag{5}$$

$$\rightleftarrows N_2 + 6O_OH + 6e^- \rightleftarrows N_2 + 3H_2O + 3O_O + 6e^- \tag{6}$$

$$\rightleftarrows 2NO + 6O_OH + 6e^- \rightleftarrows 2NO + 3H_2O + 3O_O + 10e^- \tag{7}$$

$$\rightleftarrows 2N_2O + 6O_OH + 6e^- \rightleftarrows 2N_2O + 3H_2O + 3O_O + 10e^- \tag{8}$$

All these electron donor processes increase the WO_3 conductance by injecting electrons to the conduction band.

In the present paper, to check the sensing properties of the obtained materials, WO_3 nanocrystals were homogeneously *drop-casted* onto Suprasil quartz slides to obtain films for the sensing measurements.

Fig. 7a shows the SEM image of the deposited WO_3-RE nanocrystals where it is evident that, although the increased agglomeration the nanocrystals retain their initial morphology.

The resistance of WO_3 films decreases under NH_3 while it increases under air, thus confirming the n-type semiconductor behavior. Moreover, the response of the sensing layers becomes higher as the ammonia concentration becomes higher (Fig. 7b). The electrical responses ($S = R_{AIR}/R_{MIX}$) were taken at different temperatures (200–325 °C) and for different NH_3 concentrations (9.25–74 ppm) in dry air.

Fig. 8a reports the electrical responses of WO_3 nanocrystals having different shapes, under the highest ammonia concentration ([NH_3] = 74 ppm in dry air), as a function of the operating temperature. The small rectangular nanocrystals (WO_3-RE) show the highest sensing at the lowest temperature with the remarkable S value of 4 at 200 °C. Surprisingly, though an increase of the sensitivity with the temperature is expected due to the increase of the surface reaction rate, the electrical response decreases at higher temperatures. This behavior is

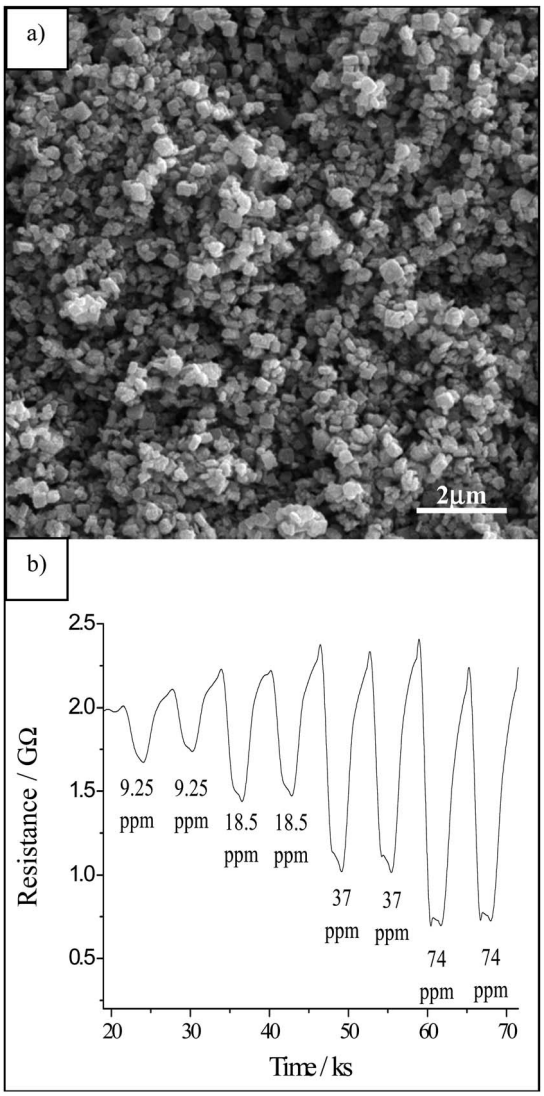

Fig. 7 (a) SEM image of WO_3-RE nanocrystals deposited by *drop-casting* onto a Suprasil quartz slide; (b) electrical resistance variation for WO_3-RE films after exposure to different concentrations of NH_3 (9.25–74 ppm) in dry air at 250 °C.

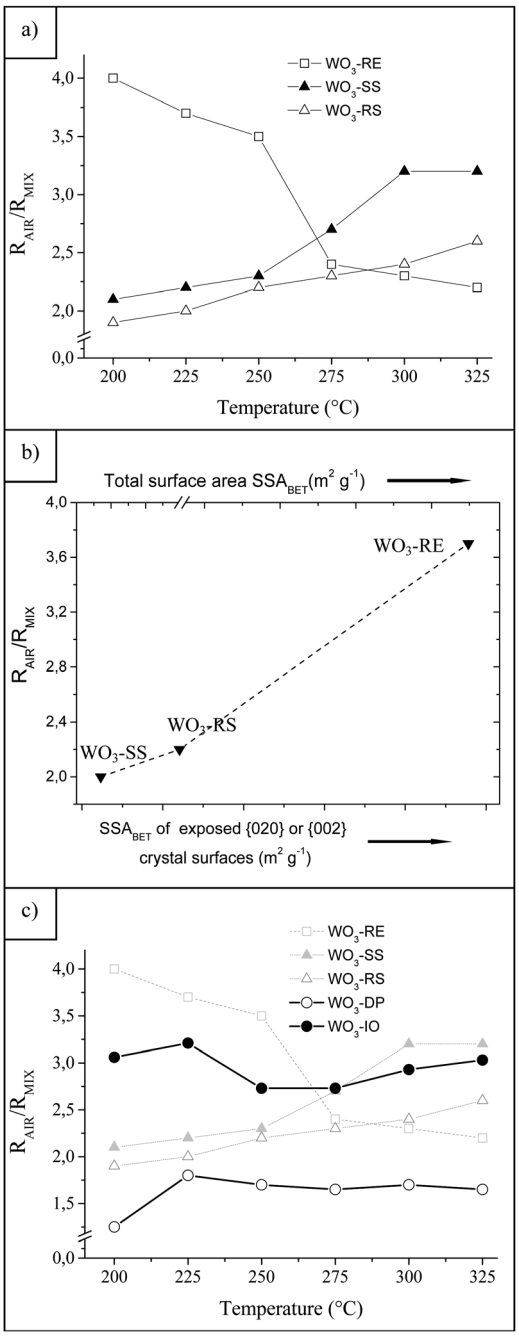

Fig. 8 (a) Electrical responses of the morphology controlled WO_3 nanocrystals as a function of the operating temperature recorded under 74 ppm [NH_3] in dry air. (b) Electrical response ($S = R_{AIR}/R_{MIX}$) of differently shaped WO_3 nanocrystals recorded under 74 ppm [NH_3] in dry air at 225 °C as a function of the total specific surface area (SSA_{BET}) and of the SSA_{BET} of their {020} and {002} exposed crystal facets. (c) Sensing performances of WO_3-IO and WO_3-DP samples with different meso/macroporous structure reported for comparison with those of shape controlled WO_3 nanoparticles under the same operating conditions.

relatable to the formation of NO on WO_3-RE sample (see XPS investigation), (reaction (7)) which easily transforms into NO_2 and acts as oxidizing agent, leading to a sensitivity decrease. The formation of NO raises with the operating temperature, thus the oxidizing effect becomes prevalent at high temperatures.[21,22]

Instead in the case of WO_3-SS and WO_3-RS nanocrystals the electrical responses between 200 and 260 °C are much lower than those of WO_3-RE nanocrystals (see Table 1) and increase with the increase of the temperature (Fig. 8a). This trend is relatable to the low amount of NO derived from the NH_3 oxidation on WO_3-SS and WO_3-RS (see XPS investigation) which generates a sensitivity trend increasing with the operating temperature.

As the sensing properties are presumably not only affected by the structure of the exposed crystal surfaces[18–24] but also by their surface area, the electrical responses of shape controlled nanocrystals under NH_3 (74 ppm)–air at 225 °C were plotted against their total SSA_{BET} and the area of their high-energy {020} and {002} exposed crystal faces (Fig. 8b).

The performances of the WO_3 nanocrystals improve as either the total surface area or the area of their high energy facets increase.

This indicates that the sensing properties of shape controlled WO_3 nanocrystals are attributable either to the exposition of high-energy surfaces or to their specific surface area.

Hence, in order to understand the relative contributions of the porous structure, of the specific surface area and of the exposed crystal facets to the sensing properties, the electrical behaviors of WO_3 inverted opal (WO_3-IO) and of the WO_3 hierarchical structures (WO_3-DP) were evaluated and compared to those of shape controlled nanocrystals (Fig. 8c). Notwithstanding the low specific surface area, the WO_3-IO macroporous film shows good sensing performance, similar or slightly lower than that observed for WO_3-RE nanocrystals, which have both high specific surface area and high SSA_{BET} of {020} facets. Unexpectedly, the meso/macroporous WO_3-DP layer with enhanced porous structure and much higher surface area, displays the worst electrical response (see Table 1).

The sensing performance of these two samples can be explained referring to their morphological features as revealed by the TEM/HRTEM investigation. The WO_3-IO (Fig. 6c and d) macroporous structure is constituted by large nanocrystals, where high-energy {020} surfaces are easily detected. On the contrary, in WO_3-DP sample the enhanced porosity, which in principle should favor the rapid and effective gas diffusion within the entire sensing layer, is instead accompanied by a disordered surface structure, and only the low-energy {200} crystal faces are noticeable.

These results suggest that the presence of high-energy faces is a fundamental requirement to upgrade the sensing properties of the WO_3 layers. Their synergistic combination of an enhanced porous structure with a targeted crystal faceting appears to be effective for developing highly sensitive WO_3 sensors. This explains the high electrical responses of WO_3-RE nanocrystals (Fig. 8) which, besides the high SSA_{BET}, greatly expose the {020} and {002} surfaces.

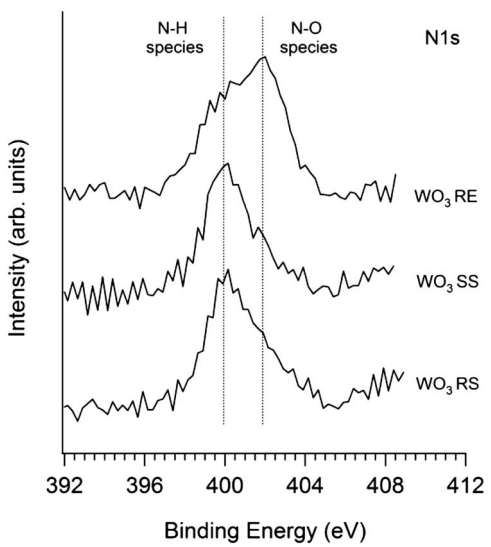

Fig. 9 XPS N1s regions for the different samples.

XPS investigation

In order to investigate the surface species which promote the ammonia oxidation (*i.e.* reactions (5)–(8)) we carried out an XPS analysis on the WO_3 drop-casted films treated in air (80 cm^3 min^{-1}) and NH_3 (74 ppm)–air (80 cm^3 min^{-1}) stream at 200 °C. Fig. 10a illustrates spectral regions pertaining to the XPS analysis of the samples. For the whole set of air-treated samples, we obtained signals from tungsten, carbon, and oxygen.

In addition to these elements, tiny amounts of nitrogen (2–6% at.) were also found for the WO_3 samples of the ammonia series. No other species were detected. In all the WO_3 samples,

Table 2 Surface parameters and sensing performances of the different WO_3 nanocrystals

Sample	N/W[a]	N–O/N–H[b]
WO_3-RE	0.29	1.13
WO_3-SS	0.10	0.32
WO_3-RS	0.09	0.38

[a] Atomic ratio as evaluated from N1s and W4f peak areas. [b] Ratio between the N1s components (N–H and N–O) as evaluated by peak fitting.

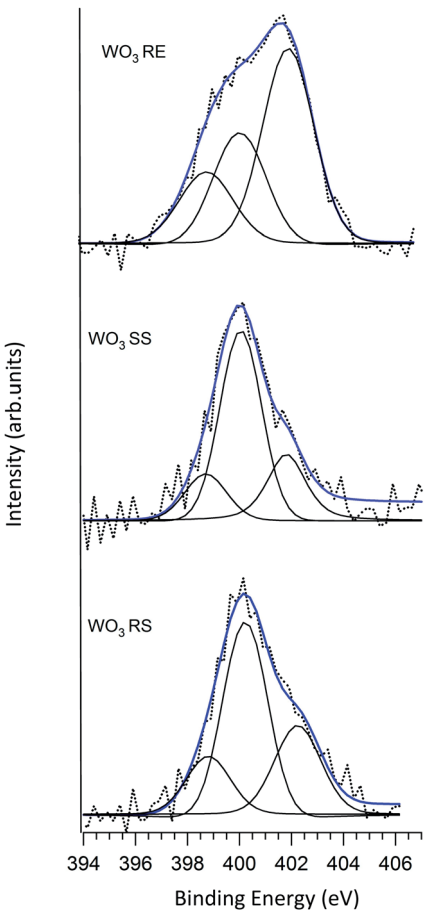

Fig. 10 XPS N1s spectra for the different WO_3 samples. The different components of the peaks are also shown.

the W4f level is characterized by a sharp doublet having a peak-to-peak separation of *ca.* 2.0 eV. The binding energy (BE) of the $W4f_{7/2}$ peak is constant to 35.9 eV, which is the typical value expected for tungsten trioxide.[37] The BE pertaining to the O1s lines agrees well with observations for the WO_3 oxygen signal, which is peaked at 530.5 eV. The N1s bandshape is broad owing to the presence of nitrogen species in different chemical environments (Fig. 9). Deconvolution of this peak allows to determine the corresponding BEs values We obtained three bands centered at 399.0 eV, 400.2 eV and 402.0 eV, within experimental uncertainty. Such values account for ammonia nitrogen atoms, surface adsorbed N–H groups, and oxidized nitrogen species, respectively.

We observed that the relative amount of the different components is dependent on the WO_3 characteristics (Table 2 and Fig. 10).

On the WO_3 surface of rectangular (WO_3-RE) nanocrystallites, oxidized nitrogen atoms represent the prevailing species, whereas N–H groups dominate in the case of rectangular platelets (WO_3-SS) and square platelets (WO_3-RS) samples. Moreover, although the intensity of the N1s region is low because of the tiny amount of nitrogen on the oxide surfaces, we estimated that the surface N/W atomic ratio on rectangular and square WO_3 platelets (SS and RS samples) is comparable ($\sim$0.1) and significantly lower than for the rectangular WO_3 (RE sample) nanocrystallites endowed with the more efficient sensing behavior (N/W $\sim$ 0.3).

These results suggest that on WO_3-RE nanocrystals with prominent high energy {020} and {002} facets the transformation of ammonia into NO species (reaction (8)) easily takes place. Subsequently NO can be easily transformed into NO_2 which acts as oxidizing agent and increases the layer resistance. The NO_2 oxidizing effect is prevalent at high temperature and justifies the descending trend of the electrical response for these samples.

Conversely, in WO_3-SS and WO_3-RS samples with very low SSA_{BET} of {020} and {002} facets the prevalence of hydrogen-rich nitrogen surface species indicates that ammonia conversion is blocked at the early stages of the reaction path (*i.e.* reaction (6)).

Based on the above considerations, it can be inferred that the high-energy {020} and {002} crystal facets can be really considered as privileged reactive sites for ammonia oxidation and ultimately drive the sensing properties of the WO_3 layers.

Conclusions

In the present study the sensing behavior towards NH_3 of WO_3 nanoparticles with specific shape and exposed surfaces, or with different meso/macroporous structure were explored and related to their morphological features, in order to evaluate the relative contributions of the oxide facets, of the porous architecture and of the specific surface area to the sensing properties. The results suggest an enhanced porous architecture and a high surface alone are not enough to guarantee a high electrical response, while the presence of {020} and {002} high-energy surfaces appears essential for an enhancement of the electrical response of the WO_3 layers. XPS investigation, performed on shape controlled WO_3 nanocrystals, allowed to better clarify the role played by these surfaces at the electronic level in the sensing mechanism and confirm the mechanism itself. It turned out that, upon interaction with NH_3, oxidized nitrogen atoms represent the prevailing species on the surface of rectangular (WO_3-RE) nanocrystals with highly exposed high-energy {020} and {002} facets, whereas N–H groups dominate in the case of rectangular platelets (WO_3-SS) and square platelets (WO_3-RS) samples with very low SSA_{BET} of these surfaces. This indicates that high energy {020} and {002} facets represent privileged reactive sites for the ammonia oxidation and ultimately drive the sensing properties of the WO_3 layers. The overall results support the idea that a cooperative interaction among highly porous structure, high surface area and targeted crystal faceting may lay the groundwork for the development of highly active WO_3 ammonia sensors.

Acknowledgements

The Milano group gratefully acknowledges the financial support of the Cariplo Foundation of Milano. The authors also personally thank Antonio Carella for his support in the experimental work and Dr Paolo Gentile for his assistance with SEM measurements. L.A. acknowledges Italian MIUR through FIRB RBPR05JH2P "Rete ItalNanoNet, FIRB RBAP114AMK "RINAME", and PRIN 20097X44S7 "Record" Projects, and the University of Padova through Progetto Strategico "HELIOS".

Notes and references

1 W. Gopel, J. Hesse and J. N. Zemel, *Sensors: a comprehensive survey*, VCH, New York, 1995, pp. 1–7.
2 *Solid-state gas sensors*, ed. P. T. Moseley and B. C. Tofield, Hilger, Bristol/Philadelphia, 1987.
3 *Gas sensors: principles, operation and developments*, ed. G. Sberveglieri, Kluwer, Boston, 1992.
4 D. Appell, *Nature*, 2002, **419**, 553.
5 L. Samuelson, *Mater. Today*, 2003, **6**, 22.
6 G. Korotcenkov, *Mater. Sci. Eng., B*, 2007, **139**, 1.
7 J. Huang and Q. Wan, *Sensors*, 2009, **9**, 9903.
8 E. Comini, C. Baratto, G. Faglia, M. Ferroni, A. Vomiero and G. Sberveglieri, *Prog. Mater. Sci.*, 2009, **54**, 1.
9 S. K. Pandey, K.-H. Kim and K.-T. Tang, *Trends Anal. Chem.*, 2012, **32**, 87.
10 X.-X. Zou, G.-D. Li, P.-P. Wang, J. Su, J. Zhao, L.-J. Zhou, Y.-N. Wang and J. S. Chen, *Dalton Trans.*, 2012, **41**, 9773.
11 G. Wang, Y. Ji, X. Huang, X. Yang, P. Gouma and M. Dudley, *J. Phys. Chem. B*, 2006, **110**, 23777.
12 M. Epifani, T. Andreu, C. R. Magana, R. Diaz, J. Arbiol, P. Siciliano and J. R. Morante, *Sens. Actuators, B*, 2010, **148**, 200.
13 A. Yan, C. Xie, D. Zeng, S. Cai and M. Hu, *Mater. Res. Bull.*, 2010, **45**, 1541.
14 M. Epifani, T. Andreu, J. Arbiol, R. Diaz, P. Siciliano and J. R. Morante, *Chem. Mater.*, 2009, **21**, 5215.
15 A. J. T. Naik, M. E. A. Warwick, S. J. A. Moniz, C. S. Blackman, I. P. Parkina and R. Binions, *J. Mater. Chem. A*, 2013, **1**, 1827.

16 C. Xu, J. Tamaki, N. Miura and N. Yamazoe, *Sens. Actuators, B*, 1991, **3**, 147.
17 I. Simon, N. Barsan, M. Bauer and U. Weimar, *Sens. Actuators, B*, 2000, **73**, 1.
18 J. H. Lee, *Sens. Actuators, B*, 2009, **140**, 319.
19 R. W. J. Scott, S. M. Yang, N. Coombs, D. E. Williams and G. A. Ozin, *Adv. Funct. Mater.*, 2003, **13**, 225.
20 H. Zheng, G. Z. Ou, M. S. Strano, R. B. Kaner, A. Mitchell and K. Kalantarzadeh, *Adv. Funct. Mater.*, 2011, **21**, 2175.
21 M. D'Arienzo, L. Armelao, C. M. Mari, S. Polizzi, R. Ruffo, R. Scotti and F. Morazzoni, *J. Am. Chem. Soc.*, 2011, **133**, 5296.
22 I. Jimenez, M. A. Centeno, R. Scotti, F. Morazzoni, J. Arbiol, A. Cornet and J. R. Morante, *J. Mater. Chem.*, 2004, **14**, 2412.
23 F. Morazzoni, R. Scotti, L. Origoni, M. D'Arienzo, I. Jimenez, A. Cornet and J. R. Morante, *Catal. Today*, 2007, **126**, 169.
24 M. D'Arienzo, M. Crippa, P. Gentile, C. M. Mari, S. Polizzi, R. Ruffo, R. Scotti, L. Wahba and F. Morazzoni, *J. Sol-Gel Sci. Technol.*, 2011, **60**, 378.
25 A. Gurlo, *Nanoscale*, 2011, **3**, 154.
26 H. Xiguang, X. Han, L. Li and C. Wang, *New J. Chem.*, 2012, **36**, 2205.
27 Y. P. Xie, G. Liu, L. Yin and H. M. Cheng, *J. Mater. Chem.*, 2012, **22**, 6746.
28 S. Rajagopal, D. Nataraj, D. Mangalaraj, Y. Djaoued, J. Robichaud and O. Y. Khyzhun, *Nanoscale Res. Lett.*, 2009, **4**, 1335.
29 L. You, Y. F. Sun, J. Ma, Y. Guan, J. M. Sun, Y. Du and G. Y. Lu, *Sens. Actuators, B*, 2011, **157**, 401.
30 J. Huang, X. Xu, C. Gu, M. Yang, M. Yang and J. Liu, *J. Mater. Chem.*, 2011, **21**, 13283.
31 R. C. Schroden, M. Al-Daous, C. F. Blanford and A. Stein, *Chem. Mater.*, 2002, **14**, 3305.
32 S. Brunauer, P. H. Emmet and E. Teller, *J. Am. Chem. Soc.*, 1938, **60**, 309.
33 E. P. Barret, L. G. Joyner and P. P. Halenda, *J. Am. Chem. Soc.*, 1951, **73**, 373.
34 D. Briggs and M. P. Seah, *Practical Surface Analysis*, J. Wiley, Chichester, 1990, vol. 1, 15.
35 G. J. A. A. Soler-Illia and C. Sanchez, *New J. Chem.*, 2000, **24**, 493.
36 R. Zhang, H. Dai, Y. Du, L. Zhang, J. Deng, Y. Xia, Z. Zhao, X. Meng and Y. Liu, *Inorg. Chem.*, 2011, **50**, 2534.
37 L. Armelao, R. Bertoncello, G. Granozzi, G. Depaoli, E. Tondello and G. Battaglin, *J. Mater. Chem.*, 1994, **4**, 407.